Amination of 1-Hexanol on Bimetallic AuPd/TiO₂ Catalysts

Amination of 1-Hexanol on Bimetallic AuPd/TiO₂ Catalysts

Madelyn R. Ball,[1][†] Thejas S. Wesley,[1][†] Keishla R. Rivera-Dones,[1] George W. Huber[1], and

James A. Dumesic[1][*]

[1] *Department of Chemical and Biological Engineering, University of Wisconsin-Madison, 1415 Engineering Drive, Madison, WI 53706*

[†] These authors contributed equally to this work.

[*] Corresponding Author: jdumesic@wisc.edu

Keywords: Bimetallic catalysts, gold, palladium, titania, amination, Fourier transform infrared spectroscopy, scanning transmission electron microscopy, X-ray absorption spectroscopy

Abstract

$AuPd/TiO_2$ catalysts, synthesized using controlled surface reactions, are active for the gas-phase amination of 1-hexanol using ammonia. The bimetallic active sites for these catalysts have been characterized using CO chemisorption and XAS techniques, and the absence of monometallic Pd species in the AuPd catalysts was confirmed using UV-vis and STEM-EDS analysis. The bimetallic catalysts exhibit synergy between Au and Pd, as the rate of hexanol conversion increases from 8.7 µmol ks^{-1} (µmol total Pd)$^{-1}$ over Pd/TiO_2 to up to 42 µmol ks^{-1} (µmol total Pd)$^{-1}$ over $AuPd/TiO_2$ with a Pd/Au atomic ratio of 0.06. The rate of hexanol conversion is also enhanced with respect to Au content, with a 5-fold increase in the total Au-normalized rate from Au/TiO_2 to $AuPd_{0.67}/TiO_2$. As Pd is added to Au/TiO_2 in increasing quantities, the production rate of primary species (i.e., hexylamine and hexanenitrile) is preferentially increased. The rate of dihexylamine production increases to a lesser extent, while trihexylamine formation remains relatively constant across Pd loadings. Moreover, trihexylamine, which cannot be formed via the condensation of dihexylamine and hexanol, is shown to be produced via the secondary aldimine, *N*-hexylidene hexylamine. The AuPd bimetallic catalysts also exhibit reduced hydrogenolysis activity compared to monometallic Pd/TiO_2.

Introduction

Amines are widely used in the chemical industry in the production of a range of useful chemicals, including pharmaceuticals, solvents, polymers, and dyes.[1–3] Typical amine syntheses are carried out using nitrile, carboxylic acid, halide, or carbonyl compounds as feedstocks, and current processes typically involve toxic species and create salt residues as a byproduct.[3–5] Thus, there exists motivation for development of more environmentally friendly processes for amine synthesis. One potentially attractive process for amine synthesis is the direct amination of alcohols to amines using ammonia. Alcohols, which are widely produced in environmentally friendly biorefinery processes, can thus be converted to amines with water formed as the only byproduct.[3–5] Thus, direct amination of alcohols offers a less toxic and more sustainable route for production of amines. This work focuses on the gas-phase amination of an aliphatic alcohol (i.e., 1-hexanol) with ammonia via "hydrogen borrowing" chemistry using $AuPd/TiO_2$ catalysts.

"Hydrogen borrowing" generally refers to atom-efficient reactions that navigate through dehydrogenated intermediates. These intermediates are subsequently reduced using hydrogen temporarily "borrowed" by the catalyst from the reactants, such that no net hydrogen is consumed.[6,7] In the case of alcohol amination, it is generally viewed that the alcohol is oxidized to its corresponding ketone or aldehyde, which undergoes nucleophilic attack by the reactant amine to form water (the only byproduct) and an imine. The imine, in turn, is hydrogenated to the product amine. This chemistry has been widely implemented in industry, with most commercial aliphatic amine syntheses relying on Co-, Ni-, Cu-, and Zr-based catalysts and ammonia as the aminating agent.[8–10]

Several studies have investigated heterogeneously-catalyzed amination of aliphatic alcohols using ammonia.[7] Shimizu et al. demonstrated the use of Ni/Al_2O_3 for the amination of

various alcohols with NH_3, achieving more than 68% selectivity to the corresponding primary amine.[3] Recently, Dumon et al. studied *n*-octanol amination using ammonia over Ni and Pd catalysts.[4] Density functional theory (DFT) calculations for the amination of methanol were carried out on Ni and Pd surfaces, and they found adsorbed ammonia to be key in predicting reactivity. The use of Ni catalysts for alcohol amination was further investigated by Tomer et al., employing a mixed metal oxide support or cyclodextrin complexes to increase conversion and selectivity to the primary amine by improving the reducibility and dispersion of nickel oxide species.[2,11] The role of Pd in amination reactivity is less well understood, and thus we have studied the impact of Pd structure on catalytic activity. Bimetallic catalysts offer an important approach to tuning the reactivity of metal catalysts, having exhibited improved or tunable reactivity, selectivity, or stability for a wide variety of reactions ranging from chemistries such as hydrogenation,[12–15] hydrogenolysis,[16–19] and hydrogen production,[20–25] to more recent efforts targeting the production of renewable chemicals and fuels via biomass upgrading[26–29] and electrochemical processes.[30–33]

The effects of bimetallic formation on amination reactions have been investigated in the literature for selected cases. Recently, Takanashi et al. demonstrated synergy between rhodium and indium for the amination of 1,2-propanediol.[34,35] The rate promotion was attributed to an electronic perturbation of rhodium sites by indium that weakens the binding of ammonia. However, they also observed reduced activity at high indium loadings, and they attributed this behavior to an ensemble effect impeding the adsorption of propanediol. Pt-Sn/γ-Al_2O_3 has also been shown to be effective for the conversion of alcohols to secondary and tertiary amines, with Sn promoting both overall reactivity as well as selectivity to amines over imines.[36,37]

Here, we use AuPd catalysts to modify the Pd structure with the goal of understanding

bimetallic effects for amination chemistry. To develop robust design principles for optimizing

multimetallic catalysts, it is necessary to understand the implications of intermetallic bonding on

the properties of catalytic surfaces and, in turn, how these features dictate surface chemistry.[38,39]

Although supported Au-Pd catalysts have not yet to our knowledge been applied to the direct

amination of aliphatic alcohols using ammonia, they have been applied to similar reactions. Ono

and Ishida investigated the amination of phenols with ammonia using Pd/Al_2O_3-based catalysts,

and they observed that addition of Au to Pd improved catalyst stability, with a negligible effect

on initial mass-specific rates.[40] More recently, Sankar, et al. employed titania-supported Au-Pd

and Ru-Pd alloy catalysts for the one-pot synthesis of *N*-benzylideneaniline and *N*-benzylaniline

from nitrobenzene and benzyl alcohol via initial transfer hydrogenation to form aniline and

benzaldehyde intermediates.[41] Both alloys were shown to be more active than monometallic Pd

for the conversion of the limiting reagent, nitrobenzene. The increased activity of Au-Pd

bimetallics was attributed to an electronic effect whereby the rate of benzyl alcohol

dehydrogenation, the suggested rate-limiting step, was increased. The high activity of Ru-Pd

catalysts was hypothesized to arise from a stabilization of Pd by the Ru in small nanoparticles.

It is generally accepted that the effects of bimetallic formation on catalysis may be

divided into two broad categories: electronic (or ligand) effects, and ensemble (or geometric)

effects.[39,42–47] Such electronic and ensemble effects have been thoroughly investigated for

bimetallic Au-Pd systems.[48] Lam, et al. observed 50-fold higher turnover frequencies (on a Pd-

basis) for AuPd than monometallic Pd for the reaction of molecular hydrogen and oxygen to

form water, and they attributed this result to weakened O binding to Pd when the latter is

coordinated to Au.[49] However, Davis and Boudart observed negligible changes in ethylene and

cyclohexene hydrogenation turnover frequencies, reaction orders, and apparent activation

energies upon the addition of Au to Pd/SiO$_2$ catalysts.[50] Due to the well-established structure-insensitivity of those hydrogenation reactions,[19,51] convolution from ensemble effects was unlikely, and thus the authors concluded that electronic effects were not important for these systems. Conversely, for reactions such as acetylene cyclization to benzene[52] and vinyl acetate synthesis,[48,53,54] ensemble effects have been shown to dominate. Still other AuPd-catalyzed reactions are susceptible to both electronic and ensemble effects, such as CO oxidation[55,56] and the direct synthesis of hydrogen peroxide.[57–60] Thus, the importance of electronic versus ensemble effects is dependent on the surface chemistry. We aim to elucidate the relative importance of electronic and ensemble effects for 1-hexanol amination using AuPd catalysts.

Here, we report reactivity and selectivity trends for a series of AuPd/TiO$_2$ catalysts for the gas-phase amination of 1-hexanol using ammonia. The catalysts were synthesized using controlled surface reactions to achieve bimetallic formation, and catalysts were characterized using CO chemisorption, Fourier transform infrared (FTIR) spectroscopy of adsorbed CO, scanning transmission electron microscopy (STEM), energy-dispersive X-ray spectroscopy (EDS), and X-ray absorption spectroscopy (XAS) techniques. We show that the addition of Pd to Au catalysts initially promotes the formation of primary products, followed by a promotion of secondary amine formation. Based on reaction kinetics studies and spectroscopic evidence, we suggest that ensemble effects likely predominate over electronic effects.

Materials and Methods

Catalyst Synthesis

A monometallic, 1 wt% Au/TiO$_2$ parent catalyst was synthesized using a deposition precipitation method, as described by Li, et al. to achieve small Au particles.[61] Briefly, TiO$_2$

(Degussa P25) was added to deionized (to a resistivity of 18.2 MΩ cm) water and stirred for 30 minutes. The pH of this slurry was adjusted to pH 10 using 0.1 M sodium hydroxide (NaOH, 97%, Sigma Aldrich) and then stirred for 90 minutes. A 0.2 M solution of gold chloride hydrate (HAuCl$_4$, 99.995%, Sigma Aldrich) containing the desired quantity of gold was added to 15 mL of 0.01 M NaOH solution and let sit for 30 minutes. The Au solution and 0.1 M NaOH were then added to the TiO$_2$ slurry simultaneously such that the pH remained constant at 10. The slurry was stirred for 2 hours, then centrifuged and washed with water. The Au/TiO$_2$ catalyst was dried in a vacuum desiccator overnight, and then reduced under flowing hydrogen (Industrial Grade, Airgas) at 623 K for 6 hours (with a heating rate of 1.5 K min) and finally passivated with flowing 1 mol% O$_2$ in He (Airgas).

Bimetallic AuPd/TiO$_2$ catalysts were synthesized using controlled surface reactions, a method developed in previous work for other multimetallic systems.[24,62–65] A portion of the Au/TiO$_2$ parent catalyst was reduced at 623 K under hydrogen flow for 6 hours (heating at 1.5 K min^{-1}) then transferred using Schlenk techniques to a glove box with an inert argon (Ultra-high purity, Airgas) atmosphere. A solution of cyclopentadienyl palladium allyl (Cp(Pd)allyl) (98%, Strem Chemicals) in n-pentane (≥99%, Sigma Aldrich) was then added to a Schlenk tube containing the Au catalyst and the slurry was stirred for 1 h. The remaining pentane was evaporated using standard Schlenk techniques. Without exposure to air, the catalyst was then reduced under flowing hydrogen at 673 K for 6 hours (with a heating rate of 1.5 K min^{-1}) and passivated with flowing 1% O$_2$ in He. Bimetallic catalysts are designated as AuPd$_x$/TiO$_2$, where x is the atomic Pd/Au ratio as measured by inductively coupled plasma-optical emission spectroscopy. The AuPd$_{0.06}$/TiO$_2$ and AuPd$_{0.23}$/TiO$_2$ catalysts were synthesized in one cycle of controlled surface reactions, while the AuPd$_{0.55}$/TiO$_2$ and AuPd$_{0.67}$/TiO$_2$ catalysts were

6

synthesized in two cycles. When multiple cycles were used, catalysts were returned to the glove box after reduction and the synthesis repeated. Equal amounts of Cp(Pd)allyl were used in each cycle to maintain a low concentration of precursor during synthesis, which, as discussed below, promotes selective bimetallic formation (as opposed to Pd deposition on the support).

A control experiment was carried out where palladium was introduced to the titania support alone. TiO_2 was treated at 623 K under hydrogen flow for 6 hours (with a heating rate of 1.5 K min^{-1}) then transferred to an inert atmosphere glovebox. Following the same procedure as described above, Cp(Pd)allyl was introduced in a *n*-pentane solution and mixed with the TiO_2, then the remaining pentane was evaporated, and the final material was treated in hydrogen.

A monometallic 0.5 wt% Pd/TiO_2 catalyst was synthesized using incipient wetness impregnation to produce a material with similar sized metal particles as the Au/TiO_2 catalyst. An aqueous solution of palladium nitrate hydrate ($Pd(NO_3)_2$, 40% Pd basis, Sigma Aldrich) was added dropwise to TiO_2 and continuously mixed until the incipient wetness point was reached. The catalyst was then dried in air overnight at 383 K, reduced under flowing hydrogen at 533 K for 6 hours (with heating rate of 1 K min^{-1}), and finally passivated with flowing 1% O_2 in He.

Characterization

UV-Visible Spectroscopy

UV-visible absorption spectra of cyclopentadienyl Pd allyl in pentane were collected using a Thermo Scientific Evolution 300 UV-visible spectrometer. Spectra were collected over wavelengths ranging from 190 to 700 nm using a 1 cm path-length quartz cuvette to contain the samples.

CO Chemisorption

The Pd dispersion was measured by CO (CP Grade, Airgas) chemisorption using a custom volumetric and gas-handling apparatus. CO was purified by passing over copper turnings at 503 K to remove metal carbonyls and 4 Å molecular sieves to remove water prior to use. Catalyst samples were reduced in flowing hydrogen (Industrial Grade, Airgas) at 533 K for 1 h (with a heating rate of 2 K min^{-1}) prior to analysis. After reduction, the samples were evacuated to 10^{-5} Torr and cooled to room temperature to collect the isotherms. CO adsorption was carried out at 293 K and the number of surface Pd atoms was taken to be equal to the irreversible CO uptake.

Fourier Transform Infrared Spectroscopy

Infrared spectra of CO adsorbed on catalyst samples were collected using a Nicolet 6700 spectrometer connected to a custom vacuum manifold. Catalyst samples were pressed into self-supporting pellets and loaded into a transmission cell described elsewhere.[66,67] Samples were reduced in flowing hydrogen (Industrial Grade, Airgas) at 573 K then cooled to room temperature and evacuated to 10^{-5} Torr. After a background scan was collected, the cell was cooled to 223 K using flowing liquid nitrogen. Then, 300 Torr of 1 mol% CO in He (Airgas) was introduced to the sample and the sample was further cooled to 103 K. Spectra of adsorbed CO were collected in the temperature range of 103 to 293 K with a resolution of 4 cm^{-1}.

Inductively Coupled Plasma-Optical Emission Spectroscopy

The total metal content of catalysts was determined using a Varian Vista-MPX CCD Simultaneous inductively coupled plasma-optical emission spectrometer (ICP-OES). Calibrations for ICP analysis were obtained by analyzing dilutions of commercial Au and Pd ICP standards (Fluka, 1000 mg L^{-1}).

Scanning Transmission Electron Microscopy – Energy Dispersive X-ray Spectroscopy

Scanning transmission electron microscopy (STEM) imaging was performed using a FEI Titan STEM with Cs aberration correction operated at 200 kV in high-angle annular dark field (HAADF) mode. Energy dispersive X-ray spectroscopy (EDS) data was collected using the same microscope with an EDAX SiLi detector. Particle composition distributions of each sample were determined by EDS analysis of at least 30 particles. Samples were prepared by dropping the passivated catalyst, suspended in ethanol, on a holey carbon coated Cu grid. The samples were plasma cleaned before loading in the microscope.

X-ray Absorption Spectroscopy

Ex-situ X-ray absorption spectroscopy (XAS) measurements were taken at beamline 10-ID at the Advanced Photon Source at Argonne National Laboratory. Measurements were taken at the Pd-K edge (24350 eV) and the Au-L_3 edge (11919 eV). Samples were pressed into wafers inside a stainless-steel sample holder, which was placed inside a quartz tube with Kapton windows on each end. The tube was flushed with helium prior to analysis and spectra were collected in transmission mode. For the catalyst with the lowest Pd loading (Pd/Au = 0.06), a poor signal-to-noise ratio at the Pd edge in transmission mode prohibited quantitative analysis of the Pd species. Spectra of Au and Pd foils were collected with each sample to calibrate the energy. Fitting of spectra was performed using the Demeter software package over an R range of 1.4-3.4 Å and a k-range of 3-10 Å^{-1}. The amplitude reduction factor was determined to be $S_0^2 = 0.82$ for Au and $S_0^2 = 0.86$ for Pd by fitting the spectra of the reference foils.

Reactivity Studies

Reactivity studies for the gas-phase amination of 1-hexanol using ammonia were conducted in a 0.7-inch OD fixed bed, borosilicate glass flow reactor operated in a down-flow configuration. In each run, the catalyst (typically between 5 and 25 mg) was diluted in 1.5 g of

silica chips (Silicon Dioxide, fused (granular), 4-20 mesh, 99.9% trace metals, Sigma-Aldrich), which had been crushed and sieved to between 106 and 212 μm to mitigate channeling artifacts. Prior to each reaction, catalysts were reduced under flowing H_2 (Industrial Grade, Airgas) at 533 K for 1 h with a heating rate of 2 K min^{-1}. All reactions were conducted at 503 K and 1 atmosphere total pressure with a gas composition of 0.07 kPa hexanol, 2.5 kPa NH_3, 51 kPa H_2, and balance He. The high H_2 pressure was required to achieve sufficiently high hexanol conversion. The reactor temperature was read using a K-type thermocouple seated in a well (which extended into the catalyst bed) in the wall of the reactor. Temperature control was achieved using a resistively heated furnace connected to a variable autotransformer supplied by a self-tuning PID process controller (Series 16A, Love Controls). To prepare the gas mixture, a flow of 20 cm^3(STP) min^{-1} hydrogen was sparged through a 1-hexanol (≥99%, Sigma-Aldrich) saturator maintained at 303 K using a heated circulating bath. A flow of 20 cm^3(STP) min^{-1} of 5 mol% NH_3 in He (Airgas) was mixed with the hexanol-saturated hydrogen stream in a tee union (heated to avoid hexanol condensation) directly upstream of the reactor. To trap all products, the reactor effluent was fed to a borosilicate glass trap filled with 1-butanol (99.9% HPLC Grade, Sigma-Aldrich) and immersed in an ice-water bath. Using a simplified variant of the method of Jou and Freeman,[68] the butanol was purified by refluxing with $NaBH_4$ (>98%, Sigma-Aldrich) (1.3 g $NaBH_4$ per L of butanol) at 323 K under bubbling Ar, followed by distillation; the middle fraction was taken for use. To quantify product formation, the reactor was periodically (approximately every 2 h) isolated, during which time the butanol-containing product trap was replaced with another equivalent one. The butanol solution from the just-removed trap was then injected on a gas chromatograph (Shimadzu GC-2010) equipped with a flame-ionization detector (hereafter referred to as GC-FID) and a Zebron ZB-50 column (30 m x 0.25 mm OD,

Phenomenex). All product identification was substantiated by comparison to analytical standards and mass spectrometry using a Shimadzu GCMS-QP2010 S. Only data reflecting steady-state catalytic reactivity are reported. All reactions were carried out at fractional hexanol conversions ranging from 16-25%; however, due to the high sensitivity of hexanol conversion to fraction-of-a-degree uncertainty in the saturator temperature, we compute total hexanol conversion rates based on the appropriate linear combination of production rates of all products observable by GC-FID and GC-MS techniques. Additionally, due to the complexity of the reaction network, we report reactivity in terms of site-time yields (STY), which are the rates at which products are formed per *defined* catalyst site (where different methods are used to count sites, as discussed below). After each reaction, the reactor was cleaned by soaking in nitric acid to be used again.

Results and Discussion

Selective Deposition of Pd

The loadings of the Au, Pd, and AuPd catalysts are shown in Table 1. Up to a Pd/Au ratio of about 0.5, the Pd/Au molar ratio as determined by ICP is in agreement with the ratio targeted during synthesis, indicating that most of the Pd introduced during the synthesis procedure was taken up by the Au/TiO_2 parent catalyst. This conclusion is corroborated by UV-vis spectra of the synthesis solutions, shown in Figure 1 and in the Supplemental Information (Figure S1). The large decrease in peaks at 260 and 320 nm after mixing the Cp(Pd)allyl solution with the reduced Au/TiO_2 parent catalyst indicates that essentially all of the Cp(Pd)allyl has been taken up by the Au/TiO_2 (Figure 1a). Furthermore, the spectra in Figure 1b indicate that the Cp(Pd)allyl was not taken up by the TiO_2 support during a control experiment, as shown by no change in the intensity of peaks at 260 and 320 nm. Because the control experiment was performed with 1.5 mg

Cp(Pd)allyl/g pentane, whereas all catalyst syntheses were carried out with precursor concentrations of at most 1.0 mg Cp(Pd)allyl/g pentane, we conclude that most of the uptake of Cp(Pd)allyl onto Au/TiO_2 during synthesis is due to Pd-Au, rather than $Pd-TiO_2$, interactions. When the concentration of precursor was increased to 3.6 mg Cp(Pd)allyl/g pentane for a control experiment, the precursor was taken up entirely by the TiO_2 support, indicating the importance of maintaining low concentrations during synthesis to achieve selective deposition of Pd onto Au.

Table 1. Compositions of Au/TiO_2, Pd/TiO_2, and $AuPd/TiO_2$ catalysts.

Catalyst	Targeted Atomic Ratio Pd/Au	ICP Atomic Ratio Pd/Au	ICP Au (wt%)	ICP Pd (wt%)
Au/TiO_2	N/A	N/A	1.09%	N/A
$AuPd_{0.06}/TiO_2$	0.05	0.06	1.06%	0.03%
$AuPd_{0.23}/TiO_2$	0.2	0.23	1.25%	0.16%
$AuPd_{0.55}/TiO_2$[a]	0.5	0.55	1.09%	0.31%
$AuPd_{0.67}/TiO_2$[a]	1	0.67	1.03%	0.37%
Pd/TiO_2	N/A	N/A	N/A	0.47%

[a] Synthesized in two cycles with equal amounts of Pd deposited during each cycle

The catalysts were also analyzed by STEM-EDS to determine particle-size distributions and qualitative compositional distributions of the individual AuPd nanoparticles. The composition distributions are shown in Supplemental Figure S2. The average composition calculated from this EDS analysis indicates a lower Pd content than that determined by ICP. This discrepancy can be attributed either to damage to the small nanoparticles by the electron beam during analysis or to large Pd particles not present in the areas observed by STEM. The likelihood of large monometallic Pd particles will be discussed further below with respect to the chemisorption and FTIR results. It is important to note, however, that on the sample areas analyzed by STEM-EDS, monometallic Pd particles were not observed and few monometallic Au particles were observed, indicating formation of AuPd bimetallic nanoparticles.
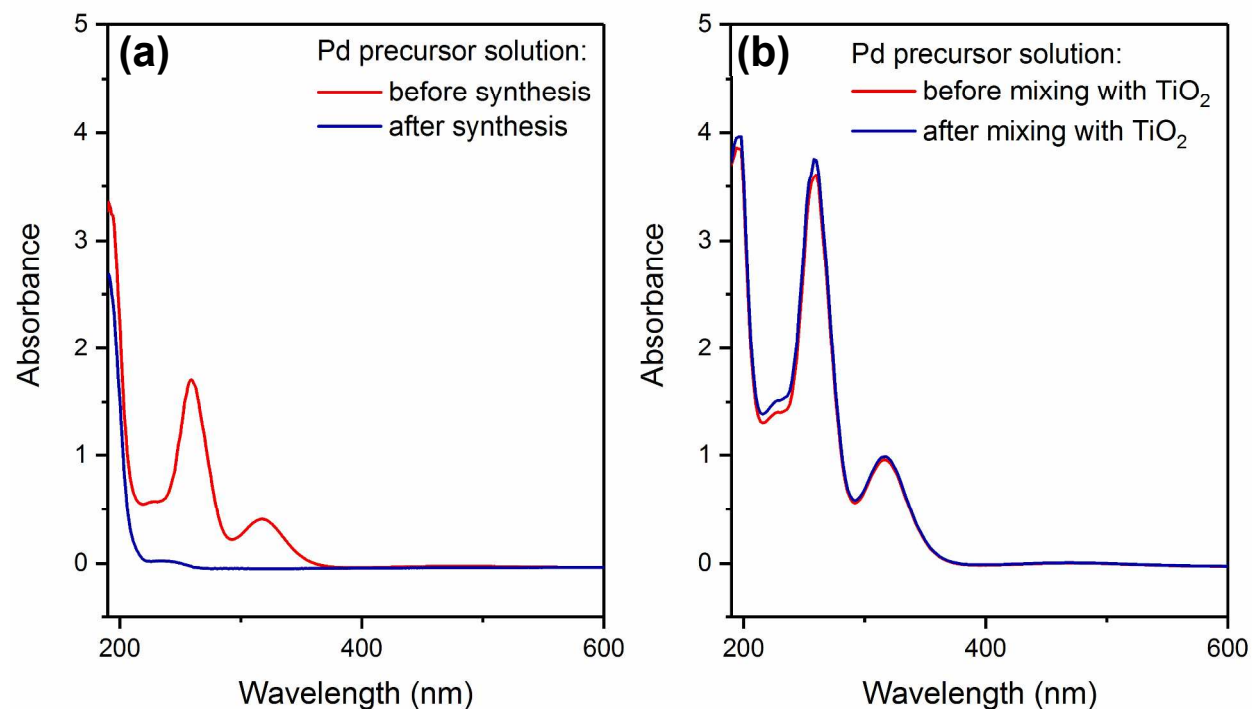
Figure 1. UV-vis spectra of Cp(Pd)allyl in pentane before (—) and after (—) contact with (a) reduced Au/TiO$_2$ catalyst during the synthesis of AuPd$_{0.23}$/TiO$_2$ and (b) TiO$_2$ as a control. Precursor concentrations were 1.0 and 1.5 mg Cp(Pd)allyl/g pentane for the synthesis (a) and control (b), respectively.

Bimetallic Catalyst Structure

Surface site densities, dispersions, and STEM-based particle sizes of the Au/TiO$_2$, Pd/TiO$_2$, and AuPd/TiO$_2$ catalysts are shown in Table 2. The Au fractional dispersion, *D*, was estimated from the Au nanoparticle sample-average diameter in nm, *d*, assuming hemispherical particles using *D = 1.16/d* as described by Bergeret and Gallezot.[69] Surface Pd was quantified using CO chemisorption assuming that the number of exposed Pd atoms was equal to the irreversible CO uptake. This stoichiometry was chosen because it has been previously reported that Pd:CO chemisorption stoichiometries are approximately 1:1 for gold-rich supported AuPd catalysts.[70] Furthermore, this stoichiometry reflects predominantly linear CO adsorption atop surface Pd atoms, which is supported by our FTIR results (see below). On monometallic Pd

catalysts, however, Pd:CO stoichiometries are known to be higher (up to Pd:CO = 2 or higher)[70] due to the presence of bridge-bonded CO.[48,55] For consistency with the bimetallic AuPd catalysts here however, we have also elected to use Pd:CO = 1:1 for Pd/TiO_2 because this assumption provides a lower bound on the monometallic Pd site density, and thus an upper bound on the monometallic Pd site-time yields and a conservative estimate for the promotional effect of bimetallic formation.

Table 2. Catalyst site densities, dispersions, and particle sizes.

Catalyst	Site Density ($\mu mol\ g^{-1}$)	Dispersion (%)	Average Particle Size[c] (nm)
Au/TiO_2	34[a]	64[a]	1.8 ± 1.4
$AuPd_{0.06}/TiO_2$	0.14[b]	4.9[b]	3.4 ± 1.7
$AuPd_{0.23}/TiO_2$	1.0[b]	6.6[b]	2.9 ± 1.5
$AuPd_{0.55}/TiO_2$	2.0[b]	7.0[b]	4.2 ± 5.1
$AuPd_{0.67}/TiO_2$	2.5[b]	7.3[b]	3.6 ± 2.4
Pd/TiO_2	7.3[b]	15[b]	1.1 ± 0.4

[a] Au surface site density and dispersion, estimated from the average particle size using $D = 1.16/d$ (Ref 72) as determined by STEM.
[b] Pd surface site density and dispersion, measured by CO chemisorption, using a Pd:CO stoichiometry of 1:1.
[c] Measured by STEM.

Under the definition of a surface site as determined by CO uptake, it is clear from Table 2 that the Pd in the bimetallic catalysts has a lower dispersion than the Pd in the monometallic Pd catalyst, and that the Pd dispersion in the bimetallic catalysts modestly decreases as Pd is increasingly diluted in Au. Because the bimetallic catalysts were reduced at a higher temperature (673 K) during synthesis than the monometallic Pd catalyst (533 K) to ensure complete decomposition of the cyclopentadienyl ligands, it was necessary to determine whether the

reduction in Pd dispersion upon bimetallic formation was caused by strong metal-support interactions (SMSI) between the Au or Pd and titania.

Strong metal-support interactions are reported to cause the migration of metal oxide species onto metal particles, potentially blocking metal sites.[71] Indeed, the chemisorptive capacity of titania-supported catalysts decreases upon reduction at temperatures as low as 573 K;[72] however, these effects may be reversed by calcining the catalyst at 673 K.[71] To determine the impact of SMSI on the AuPd/TiO$_2$ catalysts, we first calcined a portion of the AuPd$_{0.55}$/TiO$_2$ catalyst at 673 K to remove any TiO$_x$ species from the surface of the metal nanoparticles, and we subsequently reduced the sample at 533 K, the reduction temperature of the monometallic Pd/TiO$_2$. If SMSI were responsible for the lower Pd dispersion in the bimetallics, then we would expect the irreversible CO uptake on this new sample to exceed the value reported in Table 2; however, calcination had the opposite effect: CO uptake decreased to 1.1 μmol g^{-1}, likely due to sintering (Supplemental Information Table S1). To circumvent possible effects of sintering, in a second experiment the monometallic Pd/TiO$_2$ catalyst was reduced at 673 K—the reduction temperature used during bimetallic synthesis—prior to CO chemisorption, to determine if the higher-temperature reduction would induce SMSI effects and thus decrease CO uptake on the monometallic catalyst. The CO uptake on Pd/TiO$_2$ after reduction at 673 K was 5.7 μmol g^{-1}, 22% lower than the value reported in Table 2, which could be due to mild SMSI and/or particle sintering. This reduced CO uptake is consistent with the uptake reduction reported by Bracey and Burch in a similar comparison.[72] However, this effect is not sufficient to explain the factor-of-two discrepancy in dispersion between the monometallic Pd and bimetallic AuPd catalysts. We also note that work by Gubó et al. determined that a Au rich shell formed in AuPd particles with a high Au concentration which was less susceptible to SMSI than Pd rich particles.[73] Therefore,

15

while modest SMSI effects may occur in our bimetallic catalysts, they are not the primary cause of the low Pd dispersion in the bimetallics. The low dispersion of the bimetallic catalysts could be attributed to the presence of some large monometallic Pd particles, which may partially explain the difference between the EDS and ICP compositions, as discussed above. We note, however, that the dispersion of the monometallic Pd/TiO_2 catalyst (which has particles less than 2 nm in diameter) is higher than that of the bimetallic catalysts. Thus, while some large Pd particles may be present on the bimetallic catalysts, we do not expect this behavior to be the main explanation for the apparent low dispersion. We instead hypothesize that the unaccounted-for Pd is subsurface within the AuPd nanoparticles.

The preferential segregation of Au to the surface of AuPd nanoparticles is well-established in the literature, and can be the result of Au having a lower partial molar surface free energy than Pd.[48,74,75] In general, however, the surface concentration of bimetallic Au-Pd nanoparticles is dependent on the synthesis method and reaction conditions (e.g., temperature, gas composition) used.[55,75] For example, there are conditions under which Pd-rich particles have been observed to be surface-enriched in Pd.[53,76] Most notably, the segregation of Pd to the surface of bimetallic nanoparticles in the presence of CO has been well studied.[77–79] However, because of the low Pd content in the catalysts studied here, we expect that most Pd is sufficiently subsurface as to encounter prohibitively high barriers for diffusion to the nanoparticle surface, even in the presence of CO. Furthermore, work by Seemala, et al. found that the metal structure of bimetallic catalysts was influenced by the TiO_2 support.[80] In CuNi bimetallic particles, the TiO_2 support was found to induce segregation such that Cu was preferentially found on the particle surface while Ni was found at the interface with the support. This type of bimetallic segregation, induced by the differential interactions of reducible TiO_2 with the two metals, could

16

explain the low amount of surface Pd (which is more oxophilic than Au) in the AuPd particles. Other modeling work by Xu, et al. showed that the structure of AuPd particles was dependent on the redox properties of the support.[81] They determined that for particles on a TiO_2 support under reducing conditions, Pd preferred to be at the interface of the metal particle and oxide support or in the core of the particle. Thus, the subsurface Pd observed in the $AuPd/TiO_2$ catalysts used in this study can be explained based on the relative stabilities of Au and Pd in various particle configurations. Because of the Pd being primarily sub-surface or at the support interface in the bimetallic catalysts, the Pd which remains on the particle surface has a different structure than the structure found in monometallic Pd catalysts, as indicated by the FTIR results discussed below.
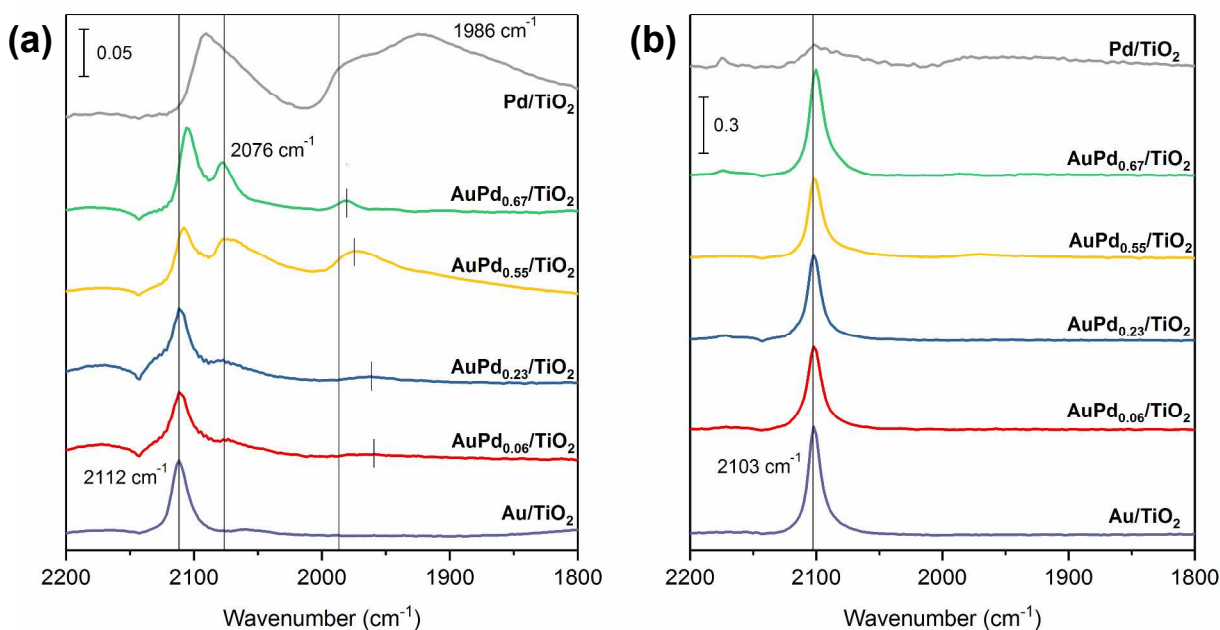
Figure 2. FTIR spectra of CO adsorbed on catalysts at (a) 283 K and (b) 153 K. The spectra were collected after introducing 300 Torr of 1 mol% CO in He.

17

Results from CO FTIR spectroscopy provide insight into the structure of the surface Pd species on the bimetallic catalysts. Figure 2 shows spectra taken at (a) 283 K and (b) 153 K after exposing the reduced catalysts to 300 Torr of 1 mol% CO in He. At low temperature, peaks corresponding to CO on Pd are not visible in the bimetallic catalysts because the Pd loadings are low and because the extinction coefficient of CO bound to Pd is much lower than that of CO bound to Au.[82,83] The peak observed at 2103 cm^{-1} for all catalysts at 153 K can be assigned to the stretching of CO bound linearly to the top of a Au atom (Figure 2b).[79] When the temperature is increased to 283 K, this peak shifts to 2112 cm^{-1} and decreases in intensity as CO desorbs from Au (Figure 2a). This blue-shift with decreasing CO coverage has been previously observed[79,84,85] and has been primarily attributed to the fact that CO chemisorption induces coverage dependent changes to the electronic band structure of Au.[85,86] This chemical effect of changing CO coverage was further shown to dominate over dipolar coupling between co-adsorbed CO molecules,[86,87] the latter of which increases CO vibrational frequency with increasing coverage.[88]

The changes in this CO-Au peak are not likely attributable to interaction with Pd, however, because the Pd/Au ratio is low such that we do not expect Pd to greatly influence bulk Au electronically. Au atoms that are locally coordinated with Pd are likely to be influenced by Pd to some extent; however, this electronic interaction is expected to affect a low fraction of Au atoms and therefore not be represented in the bulk FTIR measurement for Au.

For the monometallic Pd catalyst at room temperature (Figure 2a), we observe a peak at 2090 cm^{-1}, corresponding to linear CO on Pd.[53,79,89] A large, broad peak at 1924 cm^{-1} with a shoulder at 1986 cm^{-1} is also observed, corresponding to CO on three-fold Pd sites and bridge sites, respectively.[79,90–92] The linear CO peak at 2090 cm^{-1} for monometallic Pd/TiO$_2$ is red shifted to 2076 cm^{-1} for the AuPd bimetallic catalysts. Likewise, as Pd is increasingly diluted

18

with Au, the bridging CO peak at 1986 cm^{-1} in the monometallic Pd also shifts to lower wavenumber. This shift is consistent with the findings of Kugler and Boudart, who studied CO adsorption on AuPd/SiO$_2$ catalysts.[45] Using isotopically labelled CO to distinguish electronic alloying effects from co-adsorbate interactions, they concluded that the shift in linear-bound CO predominantly arises from electronic Au-Pd interactions, while the shift in bridge-bonded CO is primarily due to co-adsorbate interactions. Increasing Pd content is expected to lead to larger ensembles of contiguous Pd atoms and thus to more extensive CO interactions and dipolar coupling, which increases the frequency of observed vibrational modes.[55,88]

Electronic effects may be rationalized by a combined transfer of s and p electron density from Pd to Au and a concomitant, partially charge-compensating d electron transfer in the reverse direction.[38,48,75,93] Because metal-adsorbate interactions are mediated primarily by the metal d-states, as opposed to the sp-states,[94] the increased d-electron density in Pd atoms from Au coordination leads to increased occupancy of molecular orbitals exhibiting antibonding character with respect to carbon and oxygen.[95,96] The C-O bond is thus weakened, which we observe in the FTIR spectra as a red-shifted CO vibration. This observation is well-established in the literature.[45,48,92] Thus, the electronic effects induced by AuPd bimetallic formation lead to changes in the adsorption of species onto the catalyst surface.

The relative intensity of the peaks for each of the CO binding modes on Pd provides information about the surface structure of the AuPd catalysts. The monometallic Pd catalyst shows a large, broad peak between 1800-2000 cm^{-1} corresponding to the adsorption of CO on bridge and 3-fold Pd sites. For all the bimetallic catalysts, this peak corresponding to multifold CO adsorption has a much smaller area, and linear CO adsorption dominates. At low Pd loadings (Pd/Au = 0.06 and 0.23) multifold adsorption of CO is negligible, while at higher loadings

(Pd/Au = 0.55 and 0.67) a multifold CO peak is observed. The binding energy of CO on bridge and 3-fold Pd sites is stronger than the binding energy of CO on top Pd sites and thus CO adsorption is preferred on the multifold sites when available.[97,98] The low area of the multifold adsorption peak then indicates that most of the surface Pd on the bimetallic catalysts is present in isolated species surrounded by Au. The high ratio of the isolated Pd peak area to multifold Pd peak area on the bimetallic catalysts indicates a different geometric surface structure than on the monometallic Pd catalyst.

It has been reported in the literature that the interaction between Pd surface atoms is low, and as a result, Pd atoms are not likely to form clusters when no surface adsorbates are present.[77,78] When CO is present, Pd clusters are likely to form as a result of the stronger binding energy of CO on bridge Pd sites rather than top Pd sites.[78] However, the catalysts with Pd/Au = 0.06 and 0.23 do not show a multifold CO adsorption peak, which indicates that if the Pd concentration is sufficiently low, nearly all of the Pd can be isolated from other Pd atoms. This isolation may be at least partially explained by the Coulombic Pd-Pd repulsion induced by net charge transfer from Pd to Au.[48]

X-ray absorption spectroscopy on the reduced-and-passivated catalysts also provides evidence for interactions between Pd and Au in the bimetallic catalysts. Au and Pd speciation in the reduced-and-passivated catalysts was analyzed by X-ray absorption near edge spectroscopy (XANES) using a linear combination analysis, and the results are shown in Table 3. We note that some of these composition values are smaller than the corresponding error; however, this uncertainty does not affect the key conclusions from these experiments. In all of the Au-containing catalysts, Au is present as primarily metallic Au. For the Pd containing catalysts, however, Pd speciation shifts in favor of metallic Pd as the Pd/Au ratio decreases, ranging from

20

Pd^0:PdO $\cong$ 1:1 in the monometallic Pd/TiO$_2$ catalyst to Pd^0:PdO $\cong$ 9:1 for AuPd$_{0.23}$/TiO$_2$. (The

low Pd loading in AuPd$_{0.06}$/TiO$_2$ precluded this analysis for that catalyst.) The PdO species is

characteristic of surface Pd in the passivating layer, which suggests that Pd increasingly favors

migrating subsurface as the Pd loading decreases. This behavior would corroborate the low

dispersions measured by CO chemisorption.

Table 3. Fractional composition of Au and Pd oxidation states in Pd/TiO$_2$, AuPd/TiO$_2$, and Au/TiO$_2$ catalysts, as determined by XANES analysis.

Catalyst	Au L$_3$-Edge		Pd K-Edge	
	Au$_2$O$_3$	Au	PdO	Pd
Au/TiO$_2$	0.04	0.96	N/A	N/A
AuPd$_{0.06}$/TiO$_2$	0.00	1.00	a	a
AuPd$_{0.23}$/TiO$_2$	0.03	0.97	0.10	0.90
AuPd$_{0.55}$/TiO$_2$	0.03	0.97	0.27	0.73
AuPd$_{0.67}$/TiO$_2$	0.04	0.96	0.28	0.72
Pd/TiO$_2$	N/A	N/A	0.54	0.46

[a] The Pd loading in the AuPd$_{0.06}$/TiO$_2$ catalyst was too low for reliable Pd speciation.
[b] Errors for the linear combination fit are ± 2%

The EXAFS fits at both the Au and Pd edges are shown in **Error! Reference source not

found.**. For all the bimetallic catalysts, the Pd-Au coordination number is above 8 and the Pd-Pd

coordination number is less than 1.6. These values indicate that Pd is well diluted in Au, in

agreement with the results from the CO FTIR spectra. This result also suggests that

monometallic Pd particles make up a negligible portion of the bimetallic catalysts. From the Au

L$_3$-edge EXAFS analysis, we observe an increase in the Au-Pd coordination number as the Pd

content of the catalysts increases. The monometallic Pd/TiO$_2$ catalyst has a Pd-Pd coordination

number of approximately 5, which is the coordination expected for a small particle and is in

agreement with the average particle size calculated from STEM images.[99,100]

Table 4. Ex-situ EXAFS fits of the Pd K-edge and Au L$_3$-edge for Pd/TiO$_2$, AuPd/TiO$_2$, and Au/TiO$_2$ catalysts.

| Catalyst	Edge	Scatter Path	CN[a]	R[b] (Å)	Δσ^2	E$_0$ (eV)	R factor
Pd/TiO$_2$	Pd	Pd – Pd	5.4	2.73	0.008	-1.2	0.006
		Pd – O	2.3	1.92			
AuPd$_{0.67}$/TiO$_2$	Pd	Pd – Pd	1.6	2.86	0.008	13.3	0.015
		Pd – Au	11.0	2.80			
		Pd – O	0.4	1.97			
	Au	Au – Au	9.1	2.85	0.008	8.5	0.039
		Au – Pd	3.1	2.77			
		Au – O	0.2	1.97			
AuPd$_{0.55}$/TiO$_2$	Pd	Pd – Pd	1.0	2.75	0.008	13.4	0.002
		Pd – Au	8.6	2.82			
		Pd – O	1.0	2.01			
	Au	Au – Au	10.0	2.85	0.008	7.5	0.051
		Au – Pd	2.2	2.80			
		Au – O	0.6	1.98			
AuPd$_{0.23}$/TiO$_2$	Pd	Pd – Pd	1.0	2.63	0.008	12.8	0.057
		Pd – Au	10.8	2.81			
		Pd – O	0.6	2.04			
	Au	Au – Au	9.9	2.84	0.008	5.1	0.061
		Au – Pd	0.7	2.82			
		Au – O	0.5	1.90			
AuPd$_{0.06}$/TiO$_2$[c]	Au	Au – Au	10.0	2.82	0.008	4.0	0.035
		Au – Pd	0.6	2.85			
		Au – O	0.4	1.91			
Au/TiO$_2$	Au	Au – Au	8.8	2.85	0.008	5.4	0.015

Au – O	0.2	2.06

[a] Coordination number, estimated uncertainty ± 20%
[b] Distance between the absorber and back-scatterer, estimated uncertainty ± 0.02 Å
[c] Data too noisy to obtain quality fits for the Pd edge

Reactivity Trends

Scheme 1 shows a representation of the reaction network for the hydrogen borrowing-mediated amination of 1-hexanol using ammonia.[6,7] We were able to identify hexane, hexylamine, hexanenitrile, *N*-hexylidene hexylamine (the secondary aldimine), dihexylamine, and trihexylamine as products by GC-FID and GC-MS. The aldehyde (hexanal) and primary aldimine (hexylimine) intermediates were not observed by GC-FID or GC-MS techniques. We attribute their absence to their high reactivity and the large molar excess of ammonia (NH_3/hexanol = 36) used: under these conditions, any hexanal formed would react with ammonia on the catalyst surface to form the 1° aldimine since aldehyde-aldimine interconversion is typically equilibrated. The reactive 1° aldimine would then be converted to more stable products. Gaussian-based thermochemical calculations of the two-carbon analogs show that both hexanenitrile and hexylamine are favored at equilibrium (see Supplemental Information Table S2).
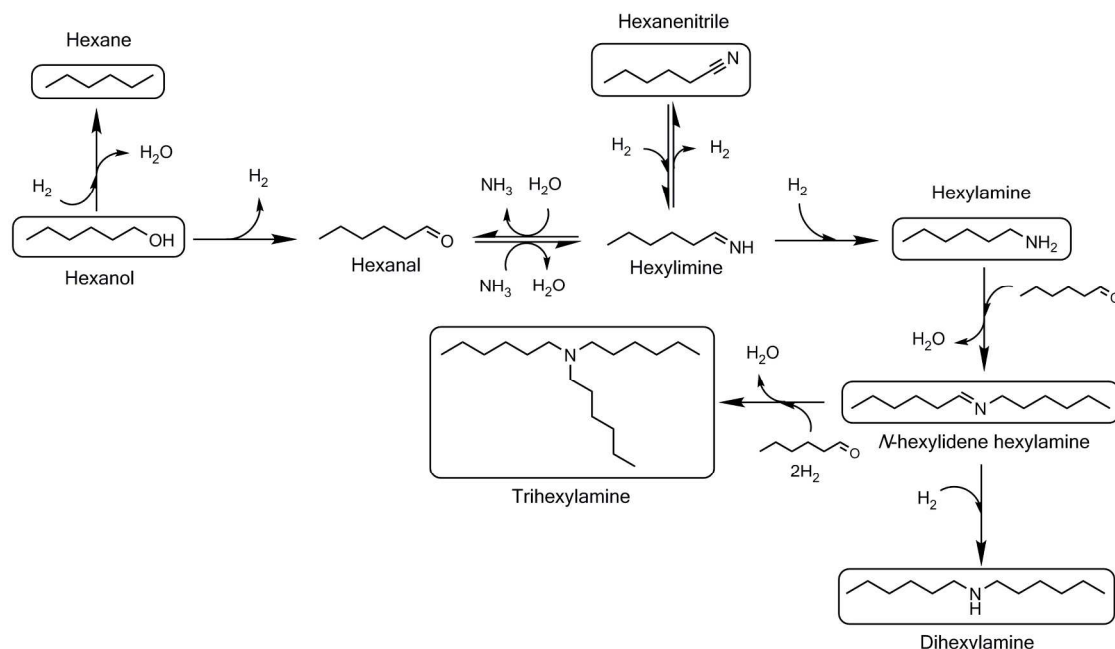
Scheme 1. Reaction network for the amination of 1-hexanol using ammonia. Boxed species were identifiable (by GC-FID and GC-MS) and quantified in this work.

Hexanol conversion rates based on product formation at 16-25% hexanol conversion are shown versus time-on-stream for the various catalysts in Supplementary Figure S3. From the time-on-stream data, it is apparent that most of the catalysts are stable over the time periods studied, typically about 8 hours. We compare catalysts using measurements after about four hours on-stream, after which point catalyst deactivation was minimal. Although ammonia and hydrogen bind more strongly to Pd than hexanol and could poison those sites, the stability of the catalyst over at least 8 hours indicates that sufficient vacant sites are available at steady state for hexanol binding.

Comparisons of the hexanol conversion rates and site-time yields (based on product formation) over the various catalysts are shown in Table 5. The rate of hexanol conversion increases from 8.7 μmol ks^{-1} (μmol total Pd)$^{-1}$ on Pd/TiO$_2$ to between 12 and 42 μmol ks^{-1} (μmol total Pd)$^{-1}$ on the bimetallic catalysts. The highest rate (per total Pd) is observed on the AuPd$_{0.06}$/TiO$_2$ catalyst, which exhibits a rate nearly 5 times higher than that over Pd/TiO$_2$.

24

Table 5. Rate of hexanol conversion and site-time yields (STY) for hexanol amination. The hexanol conversion rate is calculated as the sum of product formation rates, weighted by the number of moles of hexanol needed to form one mole of product. Conditions: 503 K, 1 atm (0.07 kPa hexanol, 2.5 kPa NH_3, 51 kPa H_2, and balance He), 16-25% hexanol conversion.

Catalyst	Rate / μmol ks^{-1} (μmol total Pd)$^{-1}$	Rate / μmol ks^{-1} (μmol total Au)$^{-1}$	Rate / μmol ks^{-1} (μmol total metal)$^{-1}$	STY / ks^{-1} [Pd sites] [a]	STY / ks^{-1} [total surface metal] [b]
Au/TiO_2	N/A	3.0	3.0	N/A	5.6
$AuPd_{0.06}/TiO_2$	42	2.2	2.1	1200	9
$AuPd_{0.23}/TiO_2$	22	5.3	4.3	340	13
$AuPd_{0.55}/TiO_2$	21	11	7.3	340	45
$AuPd_{0.67}/TiO_2$	12	7.9	4.7	300	45
Pd/TiO_2	8.7	N/A	8.7	77	12

[a] STY for AuPd and Pd catalysts calculated from surface Pd sites determined by CO chemisorption.

[b] Total surface metal site density to calculate STY was calculated using the average particle size as determined by STEM. For the Au and AuPd catalysts dispersion was calculated using *D=1.16/d* and for the Pd catalyst, *D=1.11/d* was used. (Ref. 72)

To determine the reactivity of Au in the conversion of hexanol over the bimetallic catalysts, we also calculate rates with respect to the Au metal content. The introduction of Pd to the Au parent increases the rate of hexanol conversion slightly from 3.0 μmol ks^{-1} (μmol total Au)$^{-1}$ on Au/TiO$_2$ to 5.3 μmol ks^{-1} (μmol Au)$^{-1}$ on AuPd$_{0.23}$/TiO$_2$. A further rate enhancement to 11 μmol ks^{-1} (μmol Au)$^{-1}$ is observed as the Pd loading increases to Pd/Au = 0.55. The rate decreases slightly to 7.9 μmol ks^{-1} (μmol Au)$^{-1}$ as the Pd/Au ratio is further increased to 0.67 and this trend is attributed to the higher fraction of contiguous Pd ensembles, discussed in more detail below. Thus, independently of whether the rate is normalized by total Au or Pd content, we observe an increase in activity for bimetallic catalysts over monometallic catalysts. Since the Au parent catalyst is identical for all the bimetallic catalysts, the differences in reactivity as the Pd loading changes must be attributed to changes in either the intrinsic activity of Pd or to changes in Au activity because of interaction with Pd. We note that when the rate is normalized by the total metal content, rather than surface metal, the highest rate is observed for the Pd/TiO$_2$ catalyst. This result can be attributed to the higher dispersion for this catalyst – a higher fraction of the active species is accessible.

The above results suggest that AuPd bimetallic formation creates new catalytic sites that are more active for hexanol amination than either monometallic Au or Pd sites. We note that bimetallic moieties exhibiting favorable electronic interactions and/or ensemble effects comprise the active sites regardless of whether, mechanistically, Au promotes Pd catalysis, Pd promotes Au catalysis, or both metals directly participate in the chemistry.

The coordination numbers as determined by EXAFS indicate that Pd is highly coordinated to Au, while the Au coordination to Pd is much lower. This stems from the low Pd/Au ratio, and thus each surface Pd likely exists in a bimetallic ensemble, while only a fraction

26

of the surface Au is part of a bimetallic site. Thus, we expect that the number of surface bimetallic active sites will be proportional to the number of surface Pd sites. To calculate site-time yields (for Pd-containing catalysts), we may normalize the rates by the number of Pd surface species as measured by CO chemisorption (Table 5). Based on Pd sites, the hexanol conversion STY over $AuPd_{0.06}/TiO_2$ exceeds that of Pd/TiO_2 by two orders-of-magnitude, from 77 ks^{-1} to 1200 ks^{-1}. At intermediate Pd/Au ratios ranging from 0.23 to 0.67, the STY promotion is more modest.

Site-time yields can also be calculated using site densities of total surface metal, as determined from the STEM average particle size, shown in Figure 3. For all Au containing catalysts, the total number of surface metal sites can be approximated using sites calculated by the catalyst particle size determined from STEM using $D = 1.16/d$. Similarly, the total number of surface metal sites for the Pd/TiO_2 catalyst was calculated from the Pd/TiO_2 particle size using $D=1.11/d$.[69] By this normalization, the hexanol conversion STY increases as the Pd loading in the bimetallic catalysts increases. The highest STY of 45 ks^{-1} is observed over the $AuPd_{0.55}/TiO_2$ and $AuPd_{0.67}/TiO_2$ catalysts, with total-surface STYs that are 5.6 and 3.8 times higher than that of Au/TiO_2 and Pd/TiO_2, respectively. We note that the standard deviation for the average particle size is higher on the AuPd catalysts than the monometallic Au catalyst, and thus the error in the calculated STY is also increased for the bimetallic catalysts.
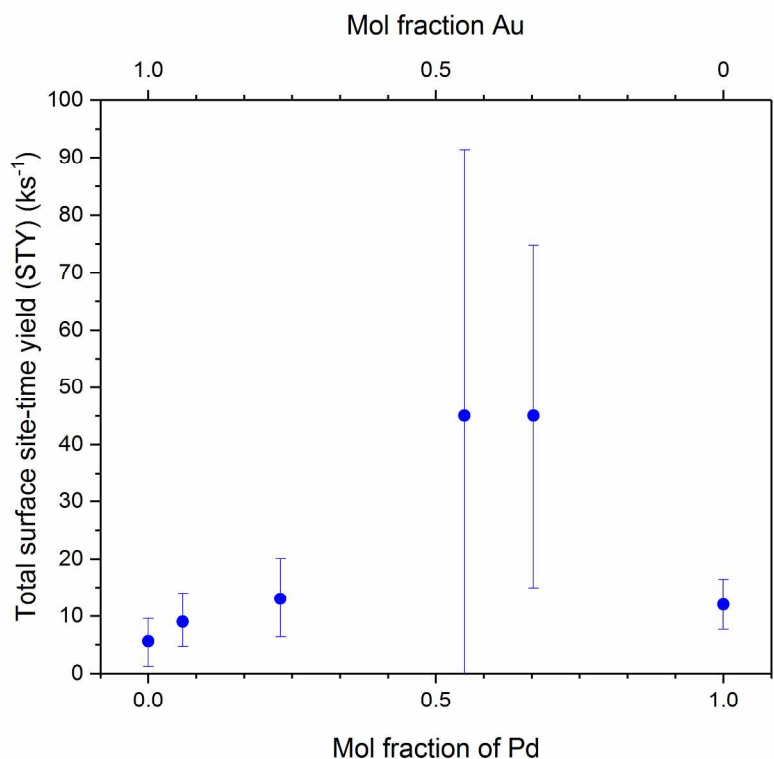
Figure 3. Total-surface site-time yield (STY) of hexanol conversion as a function of Pd and Au mol fraction. The STY values were calculated using total surface metal as estimated by the average particle size of each catalyst determined by STEM. Errors bars represent the STY calculated using sites from the average particle size ± standard deviation. Conditions: 503 K, 1 atm (0.07 kPa hexanol, 2.5 kPa NH_3, 51 kPa H_2, and balance He), 16-25% hexanol conversion.

Based on chemisorption and FTIR results, we know that the number of accessible Pd sites, which we assume to be bimetallic sites, increases with increasing Pd loading. Thus, the increase in STY when a higher fraction of the total surface sites are bimetallic sites, rather than Au sites, corroborates our conclusion that the bimetallic AuPd sites are responsible for enhanced activity. This result is in agreement with previously reported Au-Pd synergy for the AuPd/TiO$_2$-catalyzed hydrogen-borrowing amination of alcohols using nitrobenzene.[41]

Figure 4a shows the site-time yields for the formation of each product observed for the

various Au-Pd catalysts, based on total surface metal to allow for comparison of Au activity to Pd-containing catalysts. Particularly noteworthy is the presence of trihexylamine, because it cannot be formed via the previously described amination pathway: dihexylamine lacks a second nitrogen-bonded H atom, which is necessary to eliminate water from the hemiaminal adduct of hexanal and an amine to form the corresponding imine. Instead, a dehydration-hydrogenation sequence and/or a direct hydrogenolysis pathway must be kinetically accessible, and probably contributes to the formation of all three amines.
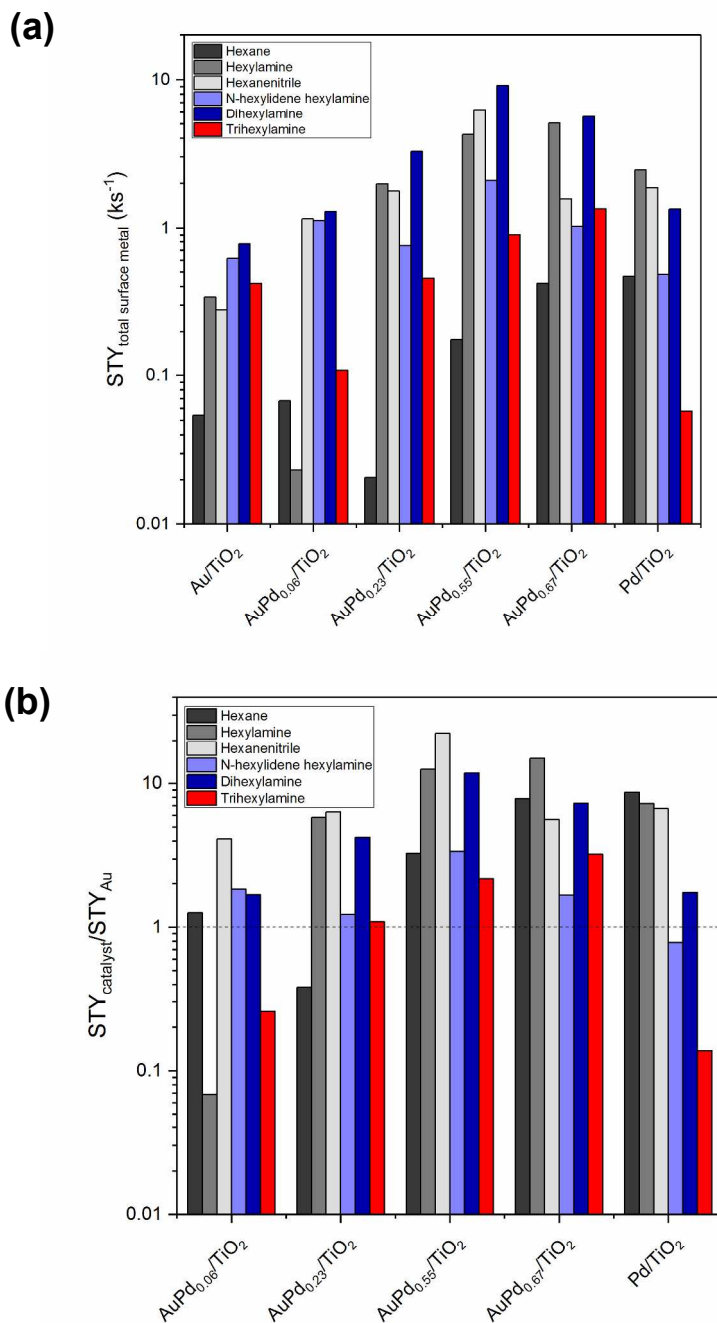
(a)

(b)

Figure 4. (a) Site-time yield of product formation based on the total surface metal of each catalyst. The total surface metal was determined using the particle size for each catalyst, and $D = 1.16/d$ for the Au containing catalysts and $D = 1.11/d$ for the Pd catalyst. (b) The rate enhancement of each product formation, as calculated by the ratio of the product site-time yield of each catalyst to the product site-time yield over Au/TiO$_2$. Conditions: 503 K, 1 atm (0.07 kPa hexanol, 2.5 kPa NH$_3$, 51 kPa H$_2$, and balance He), 16-25% hexanol conversion.

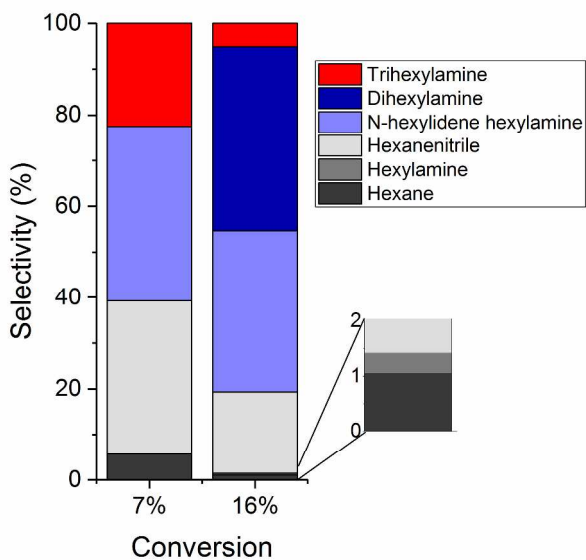**Figure 5.** Effect of hexanol conversion on product selectivity on hexanol amination product distribution for AuPd$_{0.06}$/TiO$_2$.

A comparison of product selectivity over AuPd$_{0.06}$/TiO$_2$ at 7 and 17% conversion provides insight into the formation of trihexylamine, as seen in
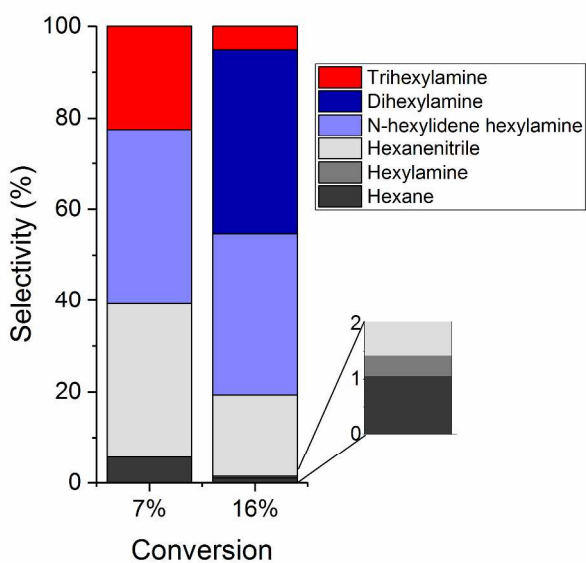
Figure 5. At lower conversion, the selectivity to hexanenitrile increases, indicating that the reaction of hexylimine to hexanenitrile is equilibrated with equilibrium favoring hexanenitrile. This result is substantiated by our Gaussian calculations, from which the equilibrium constant for hexylimine dehydrogenation to hexanenitrile is estimated to be 1.7×10^3 (Supplemental Information Table S2). The production of dihexylamine decreases to essentially zero at low conversion, while the trihexylamine selectivity increases at low conversion. This behavior indicates that trihexylamine cannot be formed via dihexylamine, but instead must pass through the 2° imine species (Scheme 1). At 7% conversion, we observe no hexylamine while at 16% conversion, the hexylamine production over the $AuPd_{0.06}/TiO_2$ catalyst is low. It is well established that the formation of imines takes place via the reaction of an aldehyde and amine[1,6,101] and thus hexylamine is necessary for the formation of *N*-hexylidene hexylamine. In this case, we can rationalize the small amount of hexylamine by its rapid conversion to further products and its low sensitivity for detection in the GC analysis. Based on these experiments, we hypothesize that hexylamine is converted to N-hexylidene hexylamine and that the formation of trihexylamine occurs via reaction of hexanal and the 2° imine.

We now consider the change in product distribution which arises from the addition of Pd to the Au parent catalyst. As Pd is added in increasing amounts to the Au parent catalyst, the rate of formation of the products increases, but not uniformly. The ratio of the STY of each product on the AuPd catalyst to the STY on the Au catalyst, i.e. the rate enhancement of product formation upon the addition of Pd, is shown in Figure 4b. As the Pd/Au ratio increases from 0.06 to 0.55, the largest enhancement in rate among the amination products is observed for the production of hexylamine and hexanenitrile. The production of dihexylamine is also enhanced as

Pd content increases, but to a lesser extent. We note that as the Pd content is further increased to

a ratio of Pd/Au = 0.67, the rate enhancement of hexanenitrile and dihexylamine decreases.

Additionally, the monometallic Pd/TiO$_2$ catalyst exhibits a higher STY for the production

of hexylamine and hexanenitrile than Au/TiO$_2$; however, the extent of rate enhancement is lower

than that of the bimetallic catalysts. Moreover, the undesirable rate of hexane production over the

Pd/TiO$_2$ catalyst is the highest of all catalysts studied. Thus, the presence of Au reduces this

undesirable hydrogenolysis activity and increases the rate of hexanol dehydrogenation to

hexanal.

The product distribution may be further analyzed by considering the selectivity trend. As
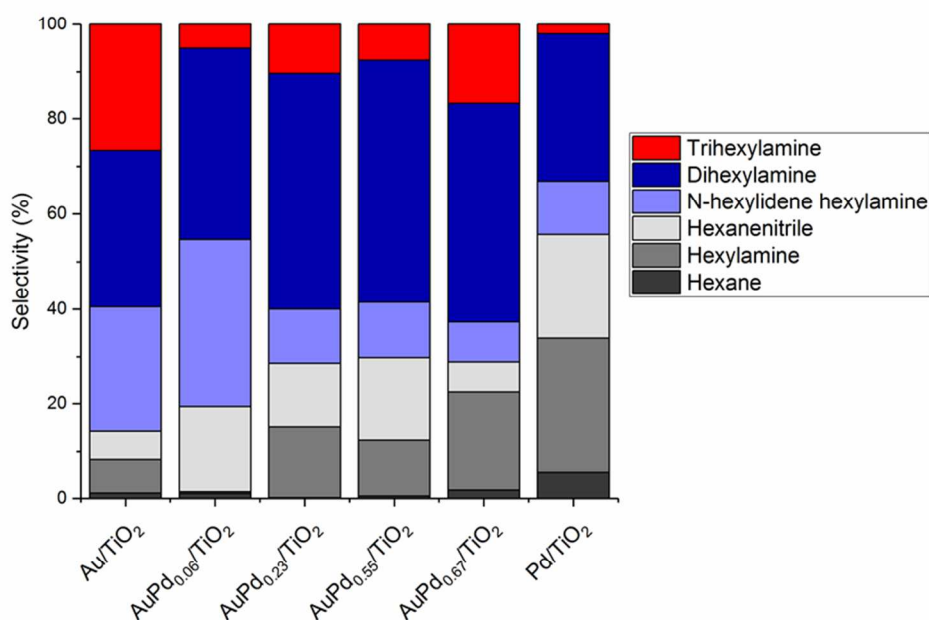
shown in

Figure 6, primary amination products are generally favored (and substituted products

disfavored) with increasing Pd fraction. This behavior is of practical interest since primary

amines are more useful than substituted amines as feedstocks for other reactions.[3,102]

Furthermore, although the hexane production rate increases with Pd content, hexane selectivity is

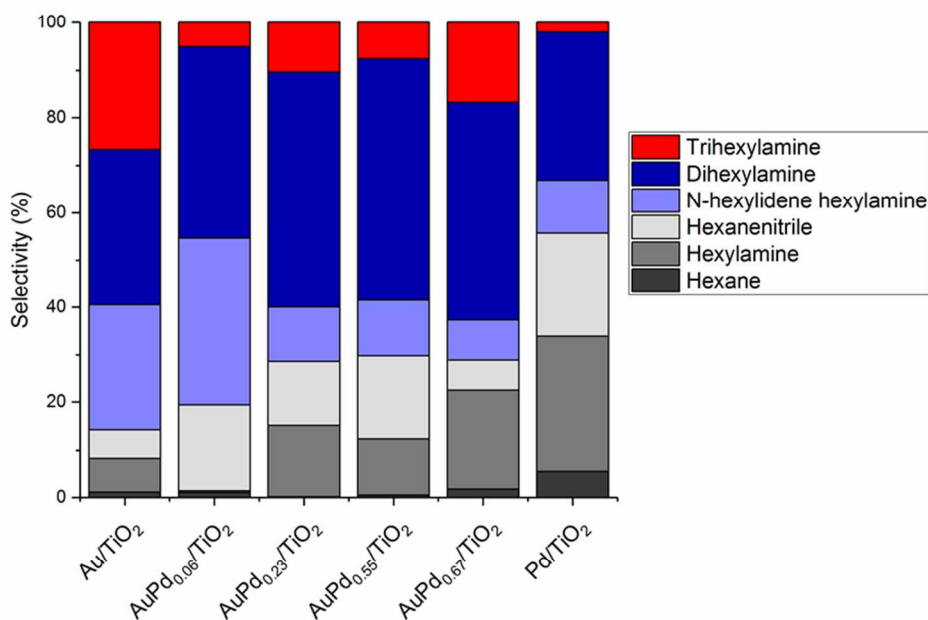maintained at ≤1.1% for all Au-containing catalysts.

Figure 6. Effect of bimetallic composition on the hexanol amination product distribution over titania-supported AuPd catalysts. Here, the selectivity of species j, S_j, is defined as $S_j = v_j R_j / \sum_k v_k R_k$; where v_j is defined as the number of hexanol molecules required to form species j (*i.e.*, 1, 2, or 3 for primary, secondary, and tertiary products, respectively), and R_j gives the production rate of species j. Primary, secondary, and tertiary products are color-coded as gray/black, blue, and red, respectively. Conditions: 503 K, 1 atm (0.07 kPa hexanol, 2.5 kPa NH_3, 51 kPa H_2, and balance He), 16-25% hexanol conversion.

Both electronic and ensemble effects have been previously reported to enhance reactivity

over AuPd catalyst systems. In our catalyst system, the position of the FTIR band for CO

adsorbed on Pd suggests an electronic interaction between Au and Pd, while the change in the

dominant binding mode for CO adsorbed on Pd also suggests a change in the geometric structure

of accessible Pd. Accordingly, both ensemble and electronic effects could induce the observed

reactivity trends. We now discuss possible explanations for these ensemble and electronic effects

in AuPd-catalyzed hexanol amination and analyze the extent to which various reaction kinetics principles can rationalize the bimetallic synergy.

The enhancement observed in the rate of hexanol conversion over the bimetallic catalysts may be attributed to geometric changes in Pd structure upon dilution in Au. From FTIR spectra of adsorbed CO, the dominant CO binding mode on the bimetallic catalysts suggests that isolated Pd species surrounded by Au are primarily present. Density functional theory calculations of methanol amination using ammonia on a Pd surface have shown that the binding energy and adsorbed structure change upon inclusion of co-adsorbed NH_3.[4] When NH_3 is present, the adsorbed intermediates form a hydrogen bond with ammonia and are thus stabilized. As a result, the activation energy for several steps increases, and the overall rate is predicted to decrease compared to a clean surface. Ammonia binds more weakly to Au than Pd. Thus, for the AuPd bimetallic catalysts with primarily isolated Pd sites, we do not expect NH_3 to bind sufficiently close to other intermediates on Pd sites to allow for formation of hydrogen bonds. As a result, the rate of hexanol conversion over AuPd catalysts is higher than the rate over a monometallic Pd catalyst, where stabilization of intermediates by co-adsorbed NH_3 is expected to occur. This behavior suggests that the geometric structure of the bimetallic AuPd catalysts is in part responsible for the enhanced rate of hexanol conversion.

The observed selectivity trend can be explained as the result of increased catalyst turnover frequency. According to transition state theory, the thermodynamic activities of reactive intermediates, rather than idealized concentrations, govern reaction rates.[103,104] It follows that for changes in catalyst composition to affect product distributions, those changes must modulate the relative activities of surface intermediates and transition states within the amination network. In the case of ammonia, if we make the assumption that adsorption is quasi-equilibrated, then the

activity of adsorbed ammonia is pinned to be equal to that of gas-phase ammonia, which is independent of catalyst composition and is fixed by the reaction conditions (temperature, pressure, and gas composition); the same principle applies to hexanol. In this respect, we can consider the rather complex amination network to consist of two phases: (1) initial hexanol dehydrogenation and ammonia adsorption, followed by (2) a pool of reactive intermediates mutually interconverting via not-necessarily-equilibrated reactions. Because surface-bound hexanal and ammonia are the only species to enter the pool, and species may only exit as one of the stable products shown in Scheme 1, the prevailing product distribution will be governed by the activities of adsorbed hexanal and ammonia (as well as relevant kinetic and thermodynamic parameters). In particular, increasing the ratio of hexanal activity to ammonia activity would increase the substitution of resultant amination products. We have already discussed that the activity of ammonia is likely to be fixed by that of the gas phase. Under steady-state operation, surface-bound hexanal is produced by hexanol dehydrogenation, and is consumed at an equal rate by the combined reactions within the reactive intermediate pool. It follows that increasing the *intrinsic* dehydrogenation rate (and thus the overall rate) will increase the number of steady-state surface-bound hexanal molecules. As a condition for thermodynamic stability,[105] this in turn raises the chemical potential (or, equivalently, activity) of adsorbed hexanal. Accompanied by an unchanged ammonia activity, the increased hexanal activity naturally leads to the formation of higher-substituted products within the reactive pool.

By comparing the Pd-based STY trend to the selectivity trend, we observe that, for the Pd-containing catalysts, increasing hexanol conversion STYs are accompanied by increasing selectivities towards secondary and tertiary products. Thus, the idea of a kinetically determined activity of surface-bound hexanal can rationalize the observed relationship between site-time

yield (our proxy for intrinsic reactivity) and product substitution.

We note that the monometallic Au/TiO$_2$ catalyst does not align with the trend predicted by the kinetically determined hexanal activity framework, since its Au-based conversion site-time yield is the lowest among all catalysts despite it producing the greatest fraction of highly substituted products. This discrepancy could be a reflection of inaccurate site-normalization on the Au/TiO$_2$ catalyst. While we have approximately normalized to the total number of surface Au atoms, Au catalysis is often mediated by just the defect sites, and smaller particles have been observed to be more active than larger ones for hydrogen borrowing amination over Au/TiO$_2$ catalysts using urea as the nitrogen source.[106] Thus, it cannot be ruled out that only a small subset of the Au defects is catalytically active, such as those vicinal to the titania support or within a particular multi-atom moiety, which could reconcile the Au/TiO$_2$ discrepancy.

Based on the overall discussion above, we suggest that geometric effects primarily govern the reactivity trend, and that the reactivity and selectivity trends may well be intrinsically coupled.

Conclusions

We have synthesized AuPd/TiO$_2$ catalysts using controlled surface reactions across a range of Pd/Au ratios. Using UV-vis spectroscopy, we have determined that Cp(Pd)allyl, the Pd precursor used in this synthesis, does not adsorb on the TiO$_2$ support at the low concentrations used during synthesis. Thus, Pd species were selectively deposited onto Au nanoparticles, forming intimate bimetallic particles. EDS analysis indicates the absence of monometallic Pd nanoparticles on the catalysts with Pd/Au ratios between 0.06 and 0.67. CO chemisorption studies indicate the AuPd nanoparticles contain Pd both on the surface and in the bulk of the

particle and infrared spectra of adsorbed CO suggest that Au influences the Pd electronically. Furthermore, compared to a monometallic Pd catalyst, CO adsorbs on the Pd in the bimetallic catalysts in a predominantly linear configuration, indicating that Pd is well dispersed in the Au. Evidence from XAS experiments also supports this conclusion.

The comparison of product distributions over $AuPd_{0.06}/TiO_2$ at different conversions indicates that trihexylamine, which cannot be formed via the condensation of hexanal and dihexylamine, is instead formed via the secondary aldimine intermediate, N-hexylidene hexylamine. Additionally, the AuPd catalysts exhibit higher hexanol conversion site-time yields than the monometallic catalysts for gas-phase hexanol amination. The formation of primary species (i.e., hexylamine and hexanenitrile) is also preferentially enhanced as Pd is increasingly added to Au. Given that CO FTIR experiments demonstrate that both electronic and ensemble effects are possible, we have used reaction kinetics principles to augment our understanding of potential Au-Pd alloying effects. On this basis, we suggest that hexanol conversion rates are primarily influenced by ensemble effects, whereas selectivity may be susceptible to both electronic and ensemble effects.

Acknowledgements

References

1   S. Bähn, S. Imm, L. Neubert, M. Zhang, H. Neumann and M. Beller, *ChemCatChem*, 2011, **3**, 1853–1864.
2   A. Tomer, Z. Yan, A. Ponchel and M. Pera-Titus, *J. Catal.*, 2017, **356**, 133–146.
3   K. I. Shimizu, K. Kon, W. Onodera, H. Yamazaki and J. N. Kondo, *ACS Catal.*, 2013, **3**, 112–117.
4   A. S. Dumon, T. Wang, J. Ibañez, A. Tomer, Z. Yan, R. Wischert, P. Sautet, M. Pera-Titus and C. Michel, *Catal. Sci. Technol.*, 2018, **8**, 611–621.
5   K. Shimizu, S. Kanno, K. Kon, S. M. A. Hakim Siddiki, H. Tanaka and Y. Sakata, *Catal. Today*, 2014, **232**, 134–138.
6   M. H. S. A. Hamid, P. A. Slatford and J. M. J. Williams, *Adv. Synth. Catal.*, 2007, **349**, 1555–1575.
7   A. Corma, J. Navas and M. J. Sabater, *Chem. Rev.*, 2018, **118**, 1410–1459.
8   P. Roose and M. G. Turcotte, *Kirk-Othmer Encycl. Chem. Technol.*, 2016, 1–20.
9   U.S. Pat, 5530127, 1996.
10   U.S. Pat, 8766009 B2, 2014.
11   A. Tomer, F. Wyrwalski, C. Przybylski, J.-F. Paul, E. Monflier, M. Pera-Titus and A. Ponchel, *J. Catal.*, 2017, **356**, 111–124.
12   G. Kyriakou, M. B. Boucher, A. D. Jewell, E. A. Lewis, T. J. Lawton, A. E. Baber, H. L. Tierney, M. Flytzani-Stephanopoulos and E. C. H. Sykes, *Science*, 2012, **335**, 1209–1212.
13   Y. Zhang, W. Diao, C. T. Williams and Monnier, *Appl. Catal. A Gen.*, 2014, **469**, 419–426.
14   T. V. Choudhary, C. Sivadinarayana, A. K. Datye, D. Kumar and D. W. Goodman, *Catal.*

Letters, 2003, **86**, 1–8.

15 B. K. Furlong, J. W. Hightower, T. Y. L. Chan, A. Sarkany and L. Guczi, *Appl. Catal. A, Gen.*, 1994, **117**, 41–51.

16 J. H. Sinfelt, J. L. Carter and D. J. C. Yates, *J. Catal.*, 1972, **24**, 283–296.

17 J. H. Sinfelt, *J. Catal.*, 1973, **29**, 308–315.

18 J. H. Sinfelt, *Acc. Chem. Res.*, 1977, **10**, 15–20.

19 J. H. Sinfelt, *Bimetallic Catalysts: Discoveries, Concepts, and Applications*, John Wiley & Sons, New York, 1983.

20 F. Besenbacher, I. Chorkendorff, B. S. Clausen, B. Hammer, A. M. Molenbroek and I. Stensgaard, *Science*, 1998, **279**, 1913–1915.

21 C. Crisafulli, S. Scirè, S. Minicò and L. Solarino, *Appl. Catal.*, 2002, **225**, 1–9.

22 D. Li, Y. Nakagawa and K. Tomishige, *Appl. Catal. A Gen.*, 2011, **408**, 1–24.

23 W. D. Williams, L. Bollmann, J. T. Miller, W. N. Delgass and F. H. Ribeiro, *Appl. Catal. B Environ.*, 2012, **125**, 206–214.

24 C. Sener, T. S. Wesley, A. C. Alba-Rubio, M. D. Kumbhalkar, S. H. Hakim, F. H. Ribeiro, J. T. Miller and J. A. Dumesic, *ACS Catal.*, 2016, **6**, 1334–1344.

25 L. Bollmann, J. L. Ratts, A. M. Joshi, W. D. Williams, J. Pazmino, Y. V. Joshi, J. T. Miller, A. J. Kropf, W. N. Delgass and F. H. Ribeiro, *J. Catal.*, 2008, **257**, 43–54.

26 T. J. Schwartz, R. L. Johnson, J. Cardenas, A. Okerlund, N. A. Da Silva, K. Schmidt-Rohr and J. A. Dumesic, *Angew. Chemie - Int. Ed.*, 2014, **53**, 12718–12722.

27 T. J. Schwartz, S. D. Lyman, A. H. Motagamwala, M. A. Mellmer and J. A. Dumesic, *ACS Catal.*, 2016, **6**, 2047–2054.

28 D. M. Alonso, S. G. Wettstein and J. A. Dumesic, *Chem. Soc. Rev.*, 2012, **41**, 8075.

29 M. Sankar, N. Dimitratos, P. J. Miedziak, P. P. Wells, C. J. Kiely and G. J. Hutchings, *Chem. Soc. Rev.*, 2012, **41**, 8099.

30 Q. Lu, G. S. Hutchings, W. Yu, Y. Zhou, R. V. Forest, R. Tao, J. Rosen, B. T. Yonemoto, Z. Cao, H. Zheng, J. Q. Xiao, F. Jiao and J. G. Chen, *Nat. Commun.*, 2015, **6**, 6567.

31 S. Xie, S. Il Choi, N. Lu, L. T. Roling, J. A. Herron, L. Zhang, J. Park, J. Wang, M. J. Kim, Z. Xie, M. Mavrikakis and Y. Xia, *Nano Lett.*, 2014, **14**, 3570–3576.

32 A. K. Singh and Q. Xu, *ChemCatChem*, 2013, **5**, 652–676.

33 J. Wu and H. Yang, *Acc. Chem. Res.*, 2013, **46**, 1848–1857.

34 T. Takanashi, Y. Nakagawa and K. Tomishige, *Chem. Lett.*, 2014, **43**, 822–824.

35 T. Takanashi, M. Tamura, Y. Nakagawa and K. Tomishige, *RSC Adv.*, 2014, **4**, 28664–28672.

36 W. He, L. Wang, C. Sun, K. Wu, S. He, J. Chen, P. Wu and Z. Yu, *Chem. - A Eur. J.*, 2011, **17**, 13308–13317.

37 K. Wu, W. He, C. Sun and Z. Yu, *Tetrahedron*, 2016, **72**, 8516–8521.

38 J. A. Rodriguez, *Surf. Sci. Rep.*, 1996, **24**, 223–287.

39 C. T. Campbell, *Annu. Rev. Phys. Chem.*, 1990, **41**, 775–837.

40 Y. Ono and H. Ishida, *J. Catal.*, 1981, **72**, 121–128.

41 M. Sankar, Q. He, S. Dawson, E. Nowicka, L. Lu, P. C. A. Bruijnincx, A. M. Beale, C. J. Kiely and B. M. Weckhuysen, *Catal. Sci. Technol.*, 2016, **6**, 5473–5482.

42 W. M. H. Sachtler, *Le Vide*, 1973, **28**, 67–71.

43 V. Ponec, *Catal. Rev. - Sci. Eng.*, 1975, **11**, 41–70.

44 W. M. H. Sachtler and R. A. Van Santen, *Adv. Catal.*, 1977, **26**, 69–119.

45 E. L. Kugler and M. Boudart, *J. Catal.*, 1979, **59**, 201–210.

46   W. M. H. Sachtler, *Faraday Discuss. Chem. Soc.*, 1981, **72**, 7–31.

47   P. Liu and J. K. Nørskov, *Phys. Chem. Chem. Phys.*, 2001, **3**, 3814–3818.

48   F. Gao and D. W. Goodman, *Chem. Soc. Rev.*, 2012, **41**, 8009.

49   Y. L. Lam, J. Criado and M. Boudart, *Nouv. J. Chim.*, 1977, **1**, 461–466.

50   R. J. Davis and M. Boudart, *Catal. Sci. Technol. Proc. First Tokyo Conf. Adv. Catal. Sci. Technol.*, 1991, 1, 129–134.

51   M. Boudart and G. Djega-Mariadassou, *Kinetics of Heterogeneous Catalytic Reactions*, Princeton University Press, 1984.

52   C. J. Baddeley, R. M. Ormerod, A. W. Stephenson and R. M. Lambert, *J. Phys. Chem.*, 1995, **99**, 5146–5151.

53   S. Simson, A. Jentys and J. A. Lercher, *J. Phys. Chem. C*, 2015, 2471–2482.

54   Y. F. Han, J. H. Wang, D. Kumar, Z. Yan and D. W. Goodman, *J. Catal.*, 2005, **232**, 467–475.

55   F. Gao, Y. Wang and D. W. Goodman, *J. Am. Chem. Soc.*, 2009, **131**, 5734–5735.

56   J. Xu, T. White, P. Li, C. He, J. Yu, W. Yuan and Y. Han, *J. Am. Chem. Soc.*, 2010, **132**, 10398–10406.

57   L. Ouyang, G. Da, P. Tian, T. Chen, G. Liang, J. Xu and Y.-F. Han, *J. Catal.*, 2014, **311**, 129–136.

58   H. C. Ham, G. S. Hwang, J. Han, S. W. Nam and T. H. Lim, *J. Phys. Chem. C*, 2007, **42**, 1465–1469.

59   F. Menegazzo, M. Signoretto, M. Manzoli, F. Boccuzzi, G. Cruciani, F. Pinna and G. Strukul, *J. Catal.*, 2009, **268**, 122–130.

60   J. K. Edwards, J. Pritchard, M. Piccinini, G. Shaw, Q. He, A. F. Carley, C. J. Kiely and G. J. Hutchings, *J. Catal.*, 2012, **292**, 227–238.

61   W. Li, M. Comotti and F. Schuth, *J. Catal.*, 2006, **237**, 190–196.

62   I. B. Aragão, I. Ro, Y. Liu, M. Ball, G. W. Huber and D. Zanchet, *Appl. Catal. B Environ.*, 2018, **222**, 1–2.

63   Y. Liu, F. Göeltl, I. Ro, M. R. Ball, C. Sener, I. B. Aragão, D. Zanchet, G. W. Huber, M. Mavrikakis and J. A. Dumesic, *ACS Catal.*, 2017, **7**, 4550–4563.

64   I. Ro, Y. Liu, M. R. Ball, D. H. K. Jackson, J. P. Chada, C. Sener, T. F. Kuech, R. J. Madon, G. W. Huber and J. A. Dumesic, *ACS Catal.*, 2016, **6**, 7040–7050.

65   S. H. Hakim, C. Sener, A. C. Alba-Rubio, T. M. Gostanian, B. J. O'Neill, F. H. Ribeiro, J. T. Miller and J. A. Dumesic, *J. Catal.*, 2015, **328**, 75–90.

66   J. Shen, J. M. Hill, R. M. Watwe, B. E. Spiewak and J. A. Dumesic, *J. Phys. Chem. B*, 1999, **103**, 3923–3934.

67   R. Carrasquillo-Flores, I. Ro, M. D. Kumbhalkar, S. Burt, C. A. Carrero, A. C. Alba-Rubio, J. T. Miller, I. Hermans, G. W. Huber and J. A. Dumesic, *J. Am. Chem. Soc.*, 2015, **137**, 10317–10325.

68   F. Y. Jou and G. R. Freeman, *J. Phys. Chem.*, 1977, **81**, 909–915.

69   G. Bergeret and P. Gallezot, in *Handbook of Heterogeneous Catalysis*, eds. G. Ertl, H. Knozinger and J. Weitkamp, VCH Verlagsgesellschaft mbH, Weinheim, 2nd edn., 1997, vol. 438, pp. 439–441.

70   X. Wei, X. F. Yang, A. Q. Wang, L. Li, X. Y. Liu, T. Zhang, C. Y. Mou and J. Li, *J. Phys. Chem. C*, 2012, **116**, 6222–6232.

71   S. J. Tauster, S. C. Fung and R. L. Garten, *J. Am. Chem. Soc.*, 1978, **100**, 170–175.

72   J. D. Bracey and R. Burch, *J. Catal.*, 1984, **86**, 384–391.

73   R. Gubó, C. M. Yim, M. Allan, C. L. Pang, A. Berkó and G. Thornton, *Top. Catal.*, 2018, **61**, 308–317.

74   A. V. Ruban, H. L. Skriver and J. K. Nørskov, *Phys. Rev. B - Condens. Matter Mater. Phys.*, 1999, **59**, 15990–16000.

75   C. W. Yi, K. Luo, T. Wei and D. W. Goodman, *J. Phys. Chem. B*, 2005, **109**, 18535–18540.

76   R. J. Davis and M. Boudart, *J. Phys. Chem.*, 1994, **98**, 5471–5477.

77   V. Soto-Verdugo and H. Metiu, *Surf. Sci.*, 2007, **601**, 5332–5339.

78   H. Y. Kim and G. Henkelman, *ACS Catal.*, 2013, **3**, 2541–2546.

79   F. Gao, Y. Wang and D. W. Goodman, *J. Phys. Chem. C*, 2009, **113**, 14993–15000.

80   B. Seemala, C. M. Cai, C. E. Wyman and P. Christopher, *ACS Catal.*, 2017, **7**, 4070–4082.

81   C. Q. Xu, M. S. Lee, Y. G. Wang, D. C. Cantu, J. Li, V. A. Glezakou and R. Rousseau, *ACS Nano*, 2017, **11**, 1649–1658.

82   A. Chiorino, M. Manzoli, F. Menegazzo, M. Signoretto, F. Vindigni, F. Pinna and F. Boccuzzi, *J. Catal.*, 2009, **262**, 169–176.

83   M. A. Vannice and S. Y. Wang, *J. Phys. Chem.*, 1981, **85**, 2543–2546.

84   D. R. Rainer, C. Xu, P. M. Holmblad and D. W. Goodman, *J. Vac. Sci. Technol. A Vacuum, Surfaces, Film.*, 1997, **15**, 1653–1662.

85   J. France and P. Hollins, *J. Electron Spectros. Relat. Phenomena*, 1993, **64–65**, 251–258.

86   P. Dumas, R. G. Tobin and P. L. Richards, *Surf. Sci.*, 1986, **171**, 579–599.

87   J. Kim, E. Samano and B. E. Koel, *J. Phys. Chem. B*, 2006, **110**, 17512–17517.

88   P. Hollins and J. Pritchard, *Prog. Surf. Sci.*, 1985, **19**, 275–349.

89   A. C. Alba-Rubio, A. Plauck, E. E. Stangland, M. Mavrikakis and J. A. Dumesic, *Catal. Letters*, 2015, **145**, 2057–2065.

90   A. M. Bradshaw and F. M. Hoffmann, *Surf. Sci.*, 1978, **72**, 513–535.

91   J. B. Giorgi, T. Schroeder, M. Bäumer and H.-J. Freund, *Surf. Sci.*, 2002, **498**, L71–L77.

92   J. Rebelli, A. A. Rodriguez, S. Ma, C. T. Williams and J. R. Monnier, *Catal. Today*, 2011, **160**, 170–178.

93   Y. F. Han, Z. Zhong, K. Ramesh, F. Chen, L. Chen, T. White, Q. Tay, S. N. Yaakub and Z. Wang, *J. Phys. Chem. C*, 2007, **111**, 8410–8413.

94   J. K. Nørskov, F. Studt, F. Abild-Pedersen and T. Bligaard, in *Fundamental Concepts in Heterogeneous Catalysis*, John Wiley & Sons, 2014, pp. 114–137.

95   G. Blyholder, *J. Phys. Chem.*, 1964, **68**, 2772–2777.

96   P. Hu, D. A. King, M. H. Lee and M. C. Payne, *Chem. Phys. Lett.*, 1995, **246**, 73–78.

97   D. Loffreda, D. Simon and P. Sautet, *Surf. Sci.*, 1999, **425**, 68–80.

98   I. V. Yudanov, R. Sahnoun, K. M. Neyman, N. Rösch, J. Hoffmann, S. Schauermann, V. Johánek, H. Unterhalt, G. Rupprechter, J. Libuda and H.-J. Freund, *J. Phys. Chem. B*, 2003, **107**, 255–264.

99   J. De Graaf, A. J. Van Dillen, K. P. De Jong and D. C. Koningsberger, *J. Catal.*, 2001, **203**, 307–321.

100   A. I. Frenkel, C. W. Hills and R. G. Nuzzo, *J. Phys. Chem. B*, 2001, **105**, 12689–12703.

101   Y. Zhang, C. S. Lim, D. S. Boon Sim, H. J. Pan and Y. Zhao, *Angew. Chemie - Int. Ed.*, 2014, **53**, 1399–1403.

102   S. Imm, L. Neubert, H. Neumann and M. Beller, *Angew. Chemie - Int. Ed.*, 2010, **49**, 8126–8129.

103   R. J. Madon and E. Iglesia, *J. Mol. Catal. A Chem.*, 2000, **163**, 189–204.
104   K. J. Laidler and M. C. King, *J. Phys. Chem.*, 1983, **87**, 2657–2664.
105   D. Chandler, *Introduction to Modern Statistical Mechanics*, Oxford University Press, New York, 1987.
106   L. He, Y. Qian, R. S. Ding, Y. M. Liu, H. Y. He, K. N. Fan and Y. Cao, *ChemSusChem*, 2012, **5**, 621–624.

Graphical Abstract:
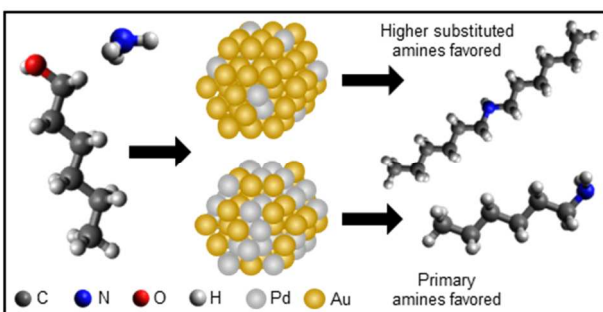
AuPd/TiO$_2$ bimetallic catalysts, synthesized using controlled surface reactions, exhibit enhanced rates for amination of hexanol using ammonia compared to monometallic Au and Pd catalysts.